Available online at www.sciencedirect.com
ScienceDirect
Journal of Power Sources 179 (2008) 164–176
JOURNAL OF POWER SOURCES
www.elsevier.com/locate/jpowsour

Transient air cooling thermal modeling of a PEM fuel cell

K.P. Adzakpa [a], J. Ramousse [a], Y. Dubé [a], H. Akremi [a], K. Agbossou [a,*], M. Dostie [b], A. Poulin [b], M. Fournier [b]

[a] *Hydrogen Research Institute and Département de génie électrique, Université du Québec à Trois-Rivières, CP 500, Trois-Rivières (QC), Canada G9A 5H7*
[b] *LTE-Hydro-Québec, 600 av. de la Montagne, Shawinigan (QC), Canada G9N 7N5K*

Received 6 November 2007; received in revised form 19 December 2007; accepted 19 December 2007
Available online 6 January 2008

Abstract

Fuel cell utilization for automobile and residential applications is a promising option in order to help reduce environmental concerns such as pollution. However, fuel cell development requires addressing their dynamic behavior to improve their performances and their life cycle. Since the temperature distribution in the cell is known to be an important factor to the fuel cell's efficiency, a cooling device is often added to homogenize the temperature in the cell and to ensure temperature control.

A 3D dynamic thermal model of a single fuel cell is presented in this work in order to study the temperature distribution in a fuel cell cooled from the bottom to the top with air. The model is governed by the thermal energy balance, taking into account the inlet gas humidity. The model is developed with the finite difference method and is implemented in the Matlab/Simulink environment. The validation is based on the performances of the "NEXA" fuel cell produced by Ballard Power Systems.

The efficiency analysis of that air cooling device reveals that the cell temperature is directly linked to the current density and to the gas humidity—varying from 30 °C at 5A to 80 °C at 35A at low humidity. Moreover, the temperature non-uniformity in the stack is shown to be very high. As a result, temperatures are higher at the top part of the cell than at the bottom part, with a difference of up to a 5 °C. Moreover the non-uniformity of the air cooling between the cells of the stack leads to large temperature variations, up to 8 °C, from one cell to another. These temperature variations result in large voltage disparities between the cells, which reduce the total electrical power of the entire stack.
© 2007 Elsevier B.V. All rights reserved.

Keywords: PEM fuel cell; 3D thermal model; Dynamic modeling; Air flow; Cooling device

1. Introduction

As an alternative to energy resource depletion and pollution problems, fuel cell systems have received much attention in research and development during the last few years. This interest has led to a good understanding of electrochemical reactions in fuel cells. Temperature, which is an important factor in the fuel cell's efficiency, has also been diversely analyzed and modeled with one to three-dimensional thermal models. Since temperature in the cell influences cell humidity, it therefore has also an indirect influence on the cell output power. It may also influence the fuel cell's durability with successive drying and flooding. A detailed understanding of the stack thermal behavior is therefore necessary for the choice of accurate cooling devices.

As noted by Berning et al. [1], the temperature distribution inside the fuel cell has important effects on nearly all transport phenomena. The authors emphasized the need to account for thermal gradients and multi-dimensional transport in fuel cells modeling. The effects on transport have also been analyzed by Yan et al. [2]. Moreover, the knowledge of the temperature increase due to irreversibilities might help in preventing failures. As reviewed by Biyikoglu [3], several works on modeling and analysis of fuel cells thermal behavior have been presented in the literature.

Many steady state models have been published [4–7]. Some [8,9] assumed a uniform temperature throughout the cell and others [10–12] present non-isothermal models. Meng [10] shows that under non-isothermal two-phase conditions, the heat trans-

* Corresponding author.
E-mail address: Kodjo.agbossou@uqtr.ca (K. Agbossou).

0378-7753/$ – see front matter © 2007 Elsevier B.V. All rights reserved.
doi:10.1016/j.jpowsour.2007.12.102

Nomenclature

A_m	membrane effective area (m^2)
C	molar concentration ($mol\,m^{-3}$)
C_p	specific heat capacity ($J\,kg^{-1}\,K^{-1}$)
$D_{A–B}$	diffusion coefficient of the gas pair A–B ($m^2\,s^{-1}$)
E_0°	thermodynamic potential at standard conditions (V)
F	Faraday's constant ($C\,mol^{-1}$)
h, h_{for}, h_{nat}	convection coefficients ($W\,m^{-2}\,K^{-1}$)
I	cell load current (A)
K, K_x, K_y, K_z	thermal conductivity coefficients ($W\,m^{-1}\,K^{-1}$)
n	number of transferred electrons in the reaction (two for H_2 and four for O_2)
N	molar flow ($mol\,m^{-2}\,s^{-1}$)
p	partial pressures (atm)
$\dot{Q}$	heat source (W)
R	universal gas constant ($J\,mol^{-1}\,K^{-1}$)
RH	relative humidity (%)
T	temperature (K)
V	voltage or overvoltage (V)

Greek letters

ε	porosity
λ	water content
ρ	density ($kg\,m^{-3}$)
σ	conductivity ($S\,m^{-1}$)

Superscripts and subscripts

act	activation
ano	anodic
cat	cathodic
cel	relating to the cell
channel	relating to the gas channel
CO	relating to CO
GDL	relating to the gas diffusion layer
H_2	relating to hydrogen
in	inlet quantity
N_2	relating to nitrogen
O_2	relating to oxygen
ohm	ohmic quantity
out	outlet quantity
op	operational quantity
r	relating to a reactant
w	relating to water

fer process significantly increases the transient response time. In his model, convection effects were neglected. Wu et al. [12] presented the same kind of results which were highly dependent on the membrane thickness. Nguyen et al. [11] also addressed non-isothermal behaviors of the cell from the point of view of water management requirements (humidification or water removal) to prevent potential membrane dehydration or electrode flooding. They showed that these requirements are much more conservative than those predicted assuming isothermal conditions. The thermal model presented by Shan and Choe [13] took into account convection as well as conduction phenomena. The authors presented a one-dimensional dynamic thermal model of a single cell based on a mass transport description. They analyzed in particular the effects of a transient temperature distribution in the cell on its electrical performances. Xue et al. [14] also presented a one-dimensional dynamic thermal model in which the convection influences are the most important factor. In their model, the PEM fuel cell is subdivided into three control volumes representing the two electrodes and the membrane. Uniform thermo-physical properties are considered throughout their work.

There exist several CFD based fuel cell models such as [15,16] for a complete analysis of thermal transfer in a single cell of PEMFC. This type of modeling gives a detailed microscopic description of the whole transport mechanisms in the cell. The thermal transient response is analyzed in Ref. [17]. Hwang et al. [18] also proposed a complete PEMFC thermal model based on a two-phase temperatures approach. They highlight the local thermal non-equilibrium between the solid matrices and the fluids. Compared to all these models, the PEM fuel cell model presented in this paper is developed for the purpose of control in a distributed power generation system. As such, the model needs to be fast running; it ought to give necessary details on the thermal behavior, but also be accurate for control.

All these above approaches address single cell modeling, although cells are actually assembled in stacks. The overall heat balance models proposed by Koh et al. [19] and Sohn et al. [20] highlight the average cell temperature variation with the operating current for air cooled stacks. They showed that the natural convection is not sufficient to keep the cell at a constant temperature. This can lead to large cell temperature variations resulting in stack voltage degradation. Additional effects of local temperatures on the voltage and power losses have been investigated by Lee et al. in Ref. [21] with a dynamic fuel cell stack model. Other dynamic models have also been published. For instance, the parametric model presented by Amphlett et al. [22] allows analyzing the dynamic thermal behavior of the stack, but they assume that the temperature is uniform. Shan and Choe [23] also addressed the transient thermal distribution in the stack. Their models characterize the dynamic response of the stack in response to external perturbations (load variations, start-up or shut down, etc.).

The main goal of the present study is to analyze the effect of the air cooling device on a PEM fuel cell stack (NEXA of Ballard). The performances of this stack were characterized by Zhu et al. [24] and del Real et al. [25] by experimental measurements of the cell voltage as a function of gas flow. In their studies, the effect of temperature on the cell voltage is emphasized, although the stack temperature is assumed uniform. Our experimental measurements of the air cooling velocities demonstrate cooling non-uniformities in the stack, which result in high temperature disparities. The measured air velocities help to define the boundary conditions of the thermal model. A three-dimensional dynamic model of a single cell is developed in order to explain further phenomena such as the cell drying or flooding, voltage

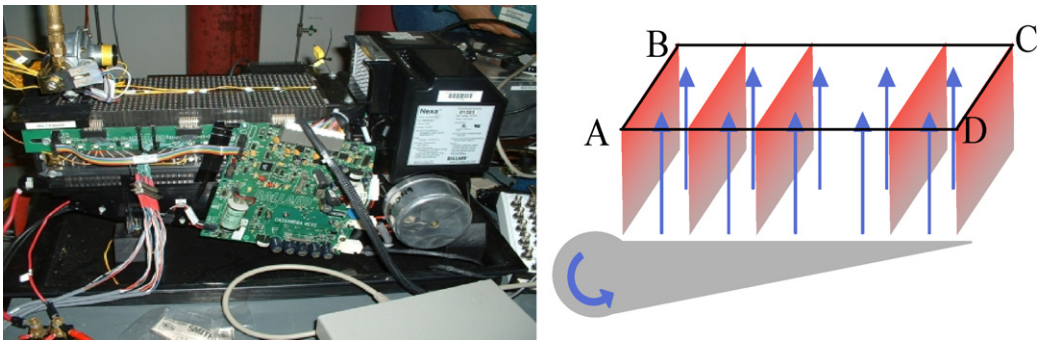

Fig. 1. Description of the modeled PEM fuel cell stack and its ventilation.

degradations, etc. The developed thermal model is based on the total thermal power produced by the electrochemical reactions. Whereas the thermal model is three-dimensional, the electrochemical model is pseudo two-dimensional; it helps to estimate heat sources in the cell. The heat transfer model includes the conduction and the heat generation phenomena inside the fuel cell, and the convection on its surface. This model helps to understand how the natural and forced convection phenomena influence the temperature field in the cell. The thermal results are presented and analyzed to prove the influence of air cooling device on the fuel cell performances.

2. Model description

2.1. Fuel cell description

The aim of this study is to analyze temperature distribution in typical air cooling fuel cells and its impact in the stack. This analysis is based on the "NEXA" fuel cell produced by Ballard Power Systems, and which contains 47 vertical cells assembled in series, and completely separated from one another by cooling channels (Fig. 1). The stack is ventilated from the bottom to the top. Both horizontal surfaces (tops and bottoms of the cells) are submitted to natural convection whereas the vertical surfaces are submitted to forced convections.

The reference axes are defined as follows (Fig. 2):

- the x-axis is along the cell's horizontal width,
- the y-axis is along the cell's vertical depth (cooling channels length),
- and the z-axis is along the cell's thickness.

2.2. Global heat source estimation

In a running fuel cell, a large part of the energy generated is dissipated as heat (approximately 50% in nominal conditions). This thermal power has to be removed from the cell by the cooling device to avoid important overheating.

The thermal power dissipated is estimated through the thermodynamic energy balance in the cell [26]:

$$\dot{Q}_{\text{heat}} = \dot{Q}_{\Delta H} - \dot{Q}_{\text{elec}} + \dot{Q}_{\text{sens}} \tag{1}$$

where $\dot{Q}_{\text{heat}}$ (W), $\dot{Q}_{\Delta H}$ (W), $\dot{Q}_{\text{elec}}$ (W) and $\dot{Q}_{\text{sens}}$ (W) are respectively the thermal power to be removed from the cell, the theoretical power produced by electrochemical reactions of the gases, the electrical power produced by the fuel cell, and the sensible heat of the gases. The last term $\dot{Q}_{\text{sens}}$ takes into account the power needed to heat the gases to the cell temperature.

The theoretical power supplied to the cell in Eq. (1) by the reacting gases is given by

$$\dot{Q}_{\Delta H} = -\frac{\Delta H_{\text{reac}}}{2F} I \tag{2}$$

where I is the load current and ΔH_{reac} is the total enthalpy supplied by these gases.

The electrical power produced in the cell is

$$\dot{Q}_{\text{elec}} = V_{\text{cell}} I \tag{3}$$

where the cell voltage V_{cell} is estimated through the electrochemical model presented later in this paper.

The sensible heat $\dot{Q}_{\text{sens}}$ represents the thermal energy variation of the gases heated in the cell. It is estimated from the difference between the thermal energy of the gases entering into the fuel cell and the thermal energy of the unused reaction gases and other gases leaving the fuel cell [22].

$$\dot{Q}_{\text{sens}} = \dot{Q}^{\text{in}}_{\text{sens}} - \dot{Q}^{\text{out}}_{\text{sens}} \tag{4}$$

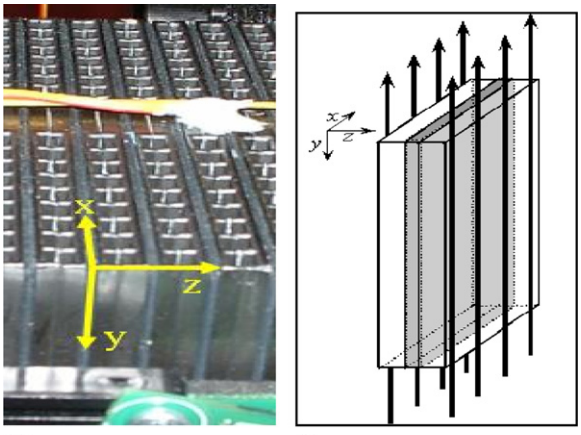

(a) (b)

Fig. 2. Reference system for the single cell modeled: (a) A cell in the stack; (b) A single ventilated cell.

In this equation, $\dot{Q}^{in}_{sens}$ and $\dot{Q}^{out}_{sens}$ are obtained through the thermodynamic energy balance [27,28] for species at the cell inlets and outlets, respectively.

$$\dot{Q}^{in}_{sens} = T^{in}_{ano}\left(C_p Q^{in}_{H_2} + C_p Q^{in}_{CO} + C_p Q^{in}_{w,ano}\right) + T^{in}_{cat}\left(C_p Q^{in}_{O_2} + C_p Q^{in}_{N_2} + C_p Q^{in}_{w,cat}\right) \quad (5)$$

$$\dot{Q}^{out}_{sens} = T^{out}_{ano}\left(C_p Q^{out}_{H_2} + C_p Q^{out}_{CO} + C_p Q^{out}_{w,ano}\right) + T^{out}_{cat}\left(C_p Q^{out}_{O_2} + C_p Q^{out}_{N_2} + C_p Q^{out}_{w,cat}\right) \quad (6)$$

In Eqs. (5) and (6), T^{in}_{ano}, T^{in}_{cat}, T^{out}_{ano} and T^{out}_{cat} are the anode and cathode inlet and outlet temperatures (K). $Q^{in}_{s,ano}$, $Q^{out}_{s,ano}$, $Q^{in}_{s,cat}$, $Q^{out}_{s,cat}$ are respectively the anode and cathode inlet and outlet molar fluxes (mol s^{-1}) of species s. C_{p_s} (J mol^{-1} K^{-1}) is the molar specific heat capacity of species s.

2.3. Dynamic thermal model

Since the aim of the dynamic thermal model is more to analyze the influence of the air cooling device on the cell than to obtain a 3D thermal description of the cell, some simplifying assumptions have to be made. This model accounts for the dissipation of the thermal power $\dot{Q}_{heat}$ from the cell (see Eq. (1)). Within the cells, only conductive heat transfer will be considered, since many authors show that convective heat transfer inside the cell is negligible [26]. The heat removal from each cell in the stack is ensured by forced convection on the lateral sides (in the x–y and y–z planes of Fig. 2) and by natural convection on both horizontal surfaces (top and bottom in the x–z plane). Because of the relatively low temperatures of operation, the heat transfer by radiation is neglected.

The structure of the stack is such as to permit the assumption that cell temperatures are independent from one cell to another. Indeed, adjacent cells are fully separated by the air cooling channels. In this case, any single cell of the stack can be simulated with its corresponding boundary conditions related to its cooling channel. Therefore, the whole stack is described as the assembly of 47 thermally independent cells.

Conductive heat transfer is described according to the Fourier equation:

$$\vec{\nabla}\cdot(K\cdot\vec{\nabla}T) = \dot{Q}_{heat} \quad (7)$$

The thermal conductivity coefficients are K_x, K_y and K_z in the x, y and z directions, respectively.

Heat transfer between the cell and the cooling channels results from convective exchanges. The boundary condition is expressed as

$$-K\cdot\vec{\nabla}T = \phi^{conv}_{nat,for} \quad (8)$$

where $\phi^{conv}_{nat,for}$ is the heat flux released by natural or forced convection, depending on the considered surface.

The thermal energy transmitted by forced convection to the air through the blades is

$$\phi^{conv}_{for} = \eta h_{for}(T_{cell} - T_{air}) \quad (9)$$

where η is the blades' efficiency, h_{for} the convection coefficient and T_{air} is the air temperature. T_{air} is estimated from experimental measurements presented in the following section.

The convection coefficient is estimated with the following correlation:

$$Nu = \frac{Dh_{for}}{K} = 1.86\left(RePr\frac{D}{L}\right)^{1/3}\left(\frac{\mu}{\mu_p}\right)^{0.14} \quad (10)$$

where Nu, Re and Pr are the Nusselt number, the Reynolds number and the Prandtl number, respectively; K and D are the thermal conductivity coefficient and the hydraulic radius.

With air ($K_{air} = 0.03$ W m^{-1} K^{-1}) flowing at 3 m s^{-1} in a 3.66×5.23 mm^2 channel, the Nusselt correlation gives $Nu \propto 5.1$, thus $h_{for} = 31.3$ W m^{-2} K^{-1}. Thus, the forced convection coefficient is set to $h_{for} = 30$ W m^{-2} K^{-1} for the simulations.

The natural convective heat flux is expressed as follows:

$$\phi^{conv}_{nat} = h_{nat}(T_{cell} - T_{amb}) \quad (11)$$

with h_{nat} set to 20% of h_{for}, $h_{nat} = 6$ W m^{-2} K^{-1}.

These values are in good agreement with the mean values of the natural convection coefficient estimated by Koh et al. [18] on a self-heated PEMFC.

In this model, the mathematical cell is subdivided into finite volumes, and the thermal balance in each control volume leads to the following discreet expression for an internal control volume (i,j,k) at time p

$$T^{p+1}_{i,j,k} = \frac{Dt}{\rho C_p}\left[k_x\frac{\left(T^p_{i-1,j,k} - 2T^p_{i,j,k} + T^p_{i+1,j,k}\right)}{Dx^2} + k_y\frac{\left(T^p_{i,j-1,k} - 2T^p_{i,j,k} + T^p_{i,j+1,k}\right)}{Dy^2} + k_z\frac{\left(T^p_{i,j,k-1} - 2T^p_{i,j,k} + T^p_{i,j,k+1}\right)}{Dz^2} + \dot{q}\right] + T^p_{i,j,k} \quad (12)$$

where Dx, Dy, Dz and Dt are respectively the finite element dimensions along the x, y and z axes and in time; C_p the specific heat capacity, ρ the cell density and $\dot{q}$ is the thermal power production rate. Depending on the position of the control volume (internal, natural convection side or forced convection side), 27 sub-cases of Eq. (12) are defined.

For sake of thermal stability due to the second law of thermodynamic, Dt is bounded

$$Dt \leq \frac{\rho C_p}{2((K_x/Dx^2) + (K_y/Dy^2) + (K_z/Dz^2) + (h_{for}/Dx) + (h_{nat}/Dy) + (h_{nat}/Dz))} \quad (13)$$

where h_{nat} and h_{for} are the natural and forced convection coefficients, respectively.

2.4. Cell electrochemical model

As presented in the previous section, the heat released in a running fuel cell is directly related to the cell voltage. It is thus necessary to properly compute the cell voltage to estimate the global heat source.

Due to the low current densities in the modeled stack, it is assumed that the concentration overvoltage is negligible, and thus the cell output voltage V_{cell} is given by

$$V_{cell} = E_{thermo} - V_{ohm} - V_{act} \tag{14}$$

The thermodynamic potential E_{thermo} resulting from the chemical reaction is obtained by the Nernst equation [26,29,30]:

$$E_{thermo} = E_0^{\circ} + (T_{op} - T_0)\left(\frac{\Delta S^{\circ}}{nF}\right) + \frac{RT_{op}}{nF}\ln\left[(p_{O_2})^{1/2}(p_{H_2})\right] \tag{15}$$

where ΔS° is the reaction entropy change at the standard temperature.

The ohmic overvoltage is

$$V_{ohm} = R_{ohm} I \tag{16}$$

where the total resistance in the cell R_{ohm} depends on the membrane characteristics, on the temperature and on its hydration levels. It is given by the following integration (17) along the membrane thickness

$$R_{ohm} = \int_0^{L_m} \frac{dx}{A_m \sigma_{T_{op}}(x)} \tag{17}$$

In this integration, $\sigma_{T_{op}}$ (S m^{-1}) is the membrane conductivity at the operational temperature T_{op}, A_m (m^2) the membrane effective area and L_m (m) is the membrane thickness. The membrane conductivity $\sigma_{T_{op}}$ depends on its temperature and on its water content, λ, expressed as the molar ratio H_2O/SO_3^-. The membrane conductivity is obtained through Eq. (18) [26,31]:

$$\sigma_{T_{op}} = 0.25 \exp\left(4.1932 - \frac{7.6138}{\lambda} + \frac{1.9796}{\lambda^2} - 1892\left(\frac{1}{T_{op}} - \frac{1}{353.15}\right)\right) \tag{18}$$

The water content distribution along the membrane thickness is estimated with the mass transport model presented below. As a result, a dryer membrane leads to higher ohmic losses.

The activation overvoltage is defined by Eq. (19) with a semi-linear parametric transformation of the Butler-Volmer equation [32]:

$$V_{act} = \xi_1 + \xi_2 T_{op} + \xi_3 T_{op} \log(c_{O_2}) + \xi_4 T_{op} \log(I) \tag{19}$$

where ξ_1, ξ_2, ξ_3 and ξ_4 depend on the cell characteristics [22,32].

The electrochemical model is strongly dependent on the temperature and on the mass transfer. In the above voltage computation, effective reactants partial pressures at the electrodes are also estimated through the mass transport model.

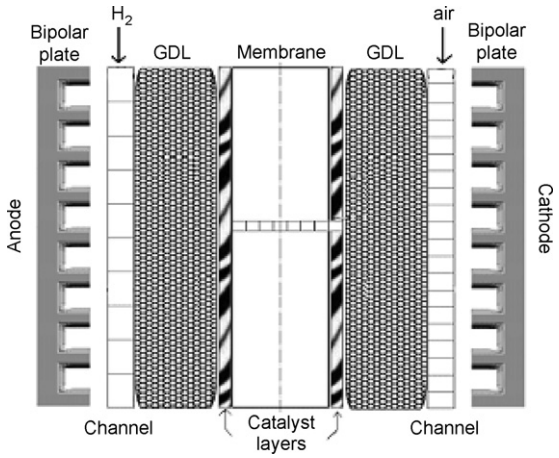

Fig. 3. . Description of the modeled PEM fuel cell.

2.5. Mass transport model

The modeled single fuel cell is fed with air and hydrogen and is schematically represented in Fig. 3. The electrochemical model is a pseudo 2D model in which the anode and cathode channels are subdivided into control volumes where the reactant concentrations are computed in order to obtain their mean concentration at the catalyst layers (see Fig. 3) [26]. Since the transient responses of the gases are clearly lower than that of liquid water in the membrane ($D_{liq}/D_{gas} \propto 10^{-4}$), gas transport is assumed to be in steady state. Therefore, the continuity equation in steady state implies that all the mass flows are uniform in the cell, for any species i

$$\vec{\nabla} N_i = 0 \tag{20}$$

The relationship between the reactive gas flows in the GDL and the load current are given by Eq. (21):

$$N_{H_2} = \frac{I}{2F}, \qquad N_{O_2} = \frac{I}{4F} \tag{21}$$

And, because the membrane is impervious to gases, the inert gas flow (impurity carbon monoxide at the anode and nitrogen at the cathode) in the GDL is null. The vapor water flow in the GDL is estimated with the mass transport model in the membrane.

2.5.1. Gas transport in the gas diffusion layer and the bipolar plates

Along their progression in the feeding channels of the bipolar plates, reactive gases are consumed at the electrodes and the resulting water must be evacuated. To model this transverse gas transport, two flow regimes are considered: the convective flow of the gases from the center of the channel to the porous gas diffusion layer (GDL), and the diffusion flow of the gases through the GDL to reach the catalyst layer.

The masses exchanged between the GDLs and the channels are modeled with a convective mass exchange coefficient

$$N_s = k(C_s^{GDL} - C_s^{channel}) \tag{22}$$

where k (m s^{-1}) is the mass transport coefficient, and C_s^{GDL} and $C_s^{channel}$ (mol m^{-3}) are respectively the concentration of

species s at the GDL/channel interface and in the feeding channel.

In the GDL, only diffusive transport is considered because of the low gases velocities. The diffusive mass flow is expressed as

$$N_s = -D_{\mathrm{w-s}} \frac{\partial C_s}{\partial z} \tag{23}$$

where $D_{\mathrm{w-s}}$ is the water vapor diffusion coefficient in species (gas) s.

The vapor water concentration at the GDL/membrane interface depends on the membrane water content via the sorption isotherm. The diffusion coefficients are computed using the Slattery and Bird's approach [33] and Bruggemann's correction [34] in order to take into account the GDL porosity.

$$D_{A-B} = \frac{1}{p} c \left(\frac{T_{\mathrm{op}}}{d} \right)^b \varepsilon^{3/2} \tag{24}$$

where $D_{\mathrm{A-B}}$ ($\mathrm{m^2\,s^{-1}}$) is the diffusion coefficient for the AB binary gas mixture, p (atm) the mixture pressure, ε the porosity of the electrode and b, c and d are gas pair-related constants.

The average concentration is computed for each species in the channels in order to estimate the mean reactants partial pressures/concentrations at the reaction site. Consequently, the effective reactants partial pressures are assumed uniform on the membrane's surface.

Finally, the partial pressures p_r of reactants r are computed from their concentration in Eq. (25):

$$p_r = C_r R T_{\mathrm{op}} \tag{25}$$

2.5.2. Water transport in the membrane

The cathodic active layer is assumed to be part of the membrane and have a measurable thickness. The water mass balance gives

$$\frac{\partial C_{\mathrm{w}}}{\partial t} + \frac{\partial N_{\mathrm{w}}}{\partial z} = \begin{cases} R_{\mathrm{H_2O}} & \text{in the cathode} \\ 0 & \text{elsewhere in the membrane} \end{cases} \tag{26}$$

where N_{w} is the water molar flow ($\mathrm{mol\,m^{-2}\,s^{-1}}$).

$R_{\mathrm{H_2O}}$ is the water generation rate ($\mathrm{mol\,m^{-3}\,s^{-1}}$) given by

$$R_{\mathrm{H_2O}} = \frac{I}{2 A_{\mathrm{m}} L_{\mathrm{cat}} F} \tag{27}$$

where L_{cat} is the cathode thickness (m), A_{m} the cell section ($\mathrm{m^2}$) and i is the current density ($\mathrm{A\,m^{-2}}$).

The water transport in the membrane is caused by three phenomena: diffusion, electro-osmotic drag and convection. Water molar flow is thus expressed as [11]

$$N_{\mathrm{w}} = -D_{\mathrm{w}} \frac{\partial C_{\mathrm{w}}}{\partial z} + \eta_{\mathrm{d}} \frac{i}{F} + C_{\mathrm{w}} v_{\mathrm{w}} \tag{28}$$

where D_{w} is the water diffusion coefficient ($\mathrm{m^2\,s^{-1}}$), η_{d} the electro-osmotic drag coefficient and v_{w} is the water velocity ($\mathrm{m\,s^{-1}}$). The water diffusion coefficient depends on the operating temperature and on the membrane hydration level [3,11].

The water drag coefficient expresses the number of water molecules pulled by each proton from the anode to the cathode. For Nafion® membranes, the following expressions are often used [9]

$$\eta_{\mathrm{d}} = \frac{2.5}{22} \lambda \tag{29}$$

$$\lambda = \frac{\mathrm{EW}}{\rho_{\mathrm{m}}} C_{\mathrm{w}} \tag{30}$$

where λ is the membrane water content (mol H_2O/mol SO_3^-), EW is the membrane equivalent weight (membrane mass (kg)/mol SO_3^-), and ρ_{m} is the density of the dry membrane ($\mathrm{kg\,m^{-3}}$). The membrane swelling is neglected.

By neglecting gravity and assuming a linear pressure drop across the membrane, the water velocity is given by [11]

$$v_{\mathrm{w}} = -\frac{K}{\mu} \frac{\partial P}{\partial z} = \frac{K}{\mu} \left(\frac{p_{\mathrm{a}} - p_{\mathrm{c}}}{L_{\mathrm{m}}} \right) \tag{31}$$

where K is the membrane permeability ($\mathrm{m^2}$), μ the water viscosity (Pa s), p_{a} and p_{c} are respectively the absolute pressure on the anode and cathode side of the membrane (Pa) and L_{m} is the membrane thickness (m).

The following second order partial derivative equation is obtained by replacing (28)–(31) in Eq. (26):

$$\frac{\partial C_{\mathrm{w}}}{\partial t} = \frac{\partial}{\partial z} \left(D_{\mathrm{w}} \frac{\partial C_{\mathrm{w}}}{\partial x} \right) - \alpha \frac{\partial C_{\mathrm{w}}}{\partial z} - \beta \frac{\partial C_{\mathrm{w}}^{\mathrm{m}}}{\partial z} + \begin{cases} 0 \\ R_{\mathrm{H_2O}} \end{cases} \quad \text{with} \quad \alpha = \frac{2.5}{22} \frac{i}{F} \frac{\mathrm{EW}}{\rho_m} \quad \text{and} \quad \beta = \frac{K}{\mu} \left(\frac{p_{\mathrm{a}} - p_{\mathrm{c}}}{L_{\mathrm{m}}} \right) \tag{32}$$

Eq. (32) is then solved using an implicit upwind finite difference scheme [11] to obtain the water concentration C_{w} and the water flows N_{w} in the whole membrane (via Eq. (28)). The boundary conditions are the water concentration $C_{\mathrm{w}}^{\mathrm{ano}}$ and $C_{\mathrm{w}}^{\mathrm{cat}}$ at the membrane interfaces. The water concentrations are converted into water content using Eq. (30).

2.5.3. Mass balance along the channel

For numerical simulation of the reactant gas flow (in the y-direction—see Fig. 3), the feeding channels are subdivided into m control volumes (40 for the oxygen channel at the cathode and 10 for the hydrogen channel at the anode) in which the mass balances are computed. Reactants inlet conditions are applied to the first control volume whereas the conditions in the last control volume correspond to those of the cell outlet.

The concentration C_r^{i+1} of reactant r in the $(i+1)$th control volume is

$$C_r^{i+1} = C_r^i - \frac{I}{nF} \frac{\Delta t}{V_{\mathrm{channel}}} \quad \text{with } \Delta t = \frac{L_{\mathrm{channel}}}{m v_{\mathrm{g}}} \tag{33}$$

where Δt is the time required for the gas flow to get across the control volume, V_{channel} ($\mathrm{m^3}$) the total volume of the channel, L_{channel} (m) the length of the channel and v_{g} ($\mathrm{m\,s^{-1}}$) is the gas velocity along the channel.

Similarly, the vapor water concentration is computed through the following equation:

$$C_{\mathrm{w}}^{i+1} = C_{\mathrm{w}}^{i} - \frac{N_{\mathrm{w}}^{i+1}\Delta t}{V_{\mathrm{channel}}/m} \tag{34}$$

Reactants mean concentrations are then computed in the channel. The current density is assumed to be uniform throughout the cell. So, given the mean concentration C_r^{mean} (mol m^{-3}) of reactant r in the channel, its effective concentration C_r at the reaction site can be computed by the following equation:

$$C_r^{\mathrm{e}} = C_r^{\mathrm{mean}} - \frac{I}{nF}\frac{2D_{\mathrm{w}-x} + L_{\mathrm{GDL}}k}{D_{\mathrm{w}-r}A_{\mathrm{m}}k} \tag{35}$$

where n is equal to two and four for hydrogen and oxygen respectively.

The flow of vapor water transferred from the electrode to the gas channel in the $(i+1)$th control volume is computed according to the following equation:

$$N_{\mathrm{w}}^{i+1} = \frac{D_{\mathrm{w}-x}A_{\mathrm{d}}k}{2D_{\mathrm{w}-x} + L_{\mathrm{GDL}}k}(C_{\mathrm{w}}^{i+1} - C_{\mathrm{w}}^{\mathrm{e}}) \tag{36}$$

where $D_{\mathrm{w-g}}$ is the water vapor diffusion coefficient in gas g, A_{d} the membrane area encompassed by the control volume, k (m s^{-1}) the mass transport coefficient, L_{GDL} (m) the GDL thickness, and $C_{\mathrm{w}}^{\mathrm{e}}$ (mol m^{-3}) is the water vapor concentration at the electrode.

3. Results and discussion

3.1. Experimental set-up

In the PEM fuel cell thermal model, each cell has the geometry shown in Fig. 4.

The grey part is composed of a 0.2 mm thick membrane, two 0.05 mm thick catalyst layers and two 0.5 mm thick diffusion layers. The equivalent thermal properties of the whole cell are estimated with the thermal properties of each material, according to the literature review presented in [35]. Thus, the through-plane thermal conductivity of the cell is set to $K_z = 0.17$ W m^{-1} K^{-1}. The in-plane thermal conductivity ($K_x = K_y = 0.85$ W m^{-1} K^{-1}) is chosen five times greater than the through-plane one's to represent the thermal anisotropy of these materials [35,36]. Moreover, the cell has an average density of 2200 kg m^{-3} and a 710 J kg^{-1} K^{-1} specific heat capacity. The two other vertical parts represent the 1.6 mm thick blades and are assumed to be in aluminium [7]. Their density and specific heat capacity are 2707 kg m^{-3} and 896 J kg^{-1} K^{-1}, respectively.

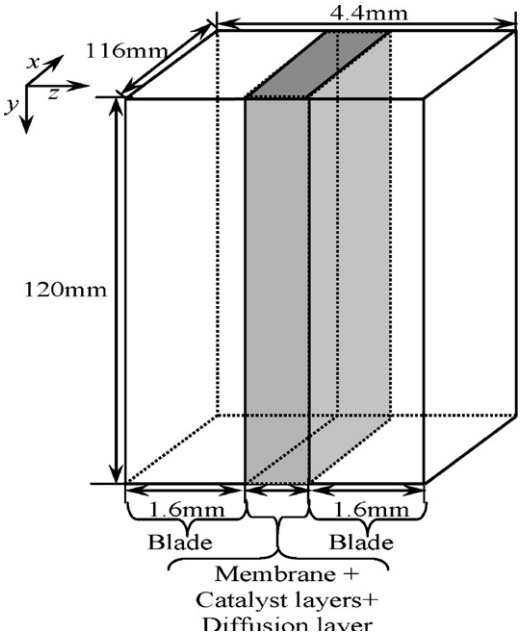

Fig. 4. Single cell geometry.

According to the heat source estimation presented previously, the thermal power to remove from the cell versus the load current is plotted in Fig. 5 with 10% and 90% relative humidity of the inlet gases. In Fig. 5, $\mathrm{RH_{ano}}$ and $\mathrm{RH_{cath}}$ are respectively the anode and cathode inlet gas relative humidity. For any current, the sensible heat ($\dot{Q}_{\mathrm{sens}}$) is less than 1 W in both cases and has a reduced influence on the thermal power to remove from the cell. On the other hand, the gas humidification has a significant impact on fuel cell performances due to its large effect on the membrane resistance. The thermal power versus the load current is summarized in Fig. 5 for low and high relative humidity

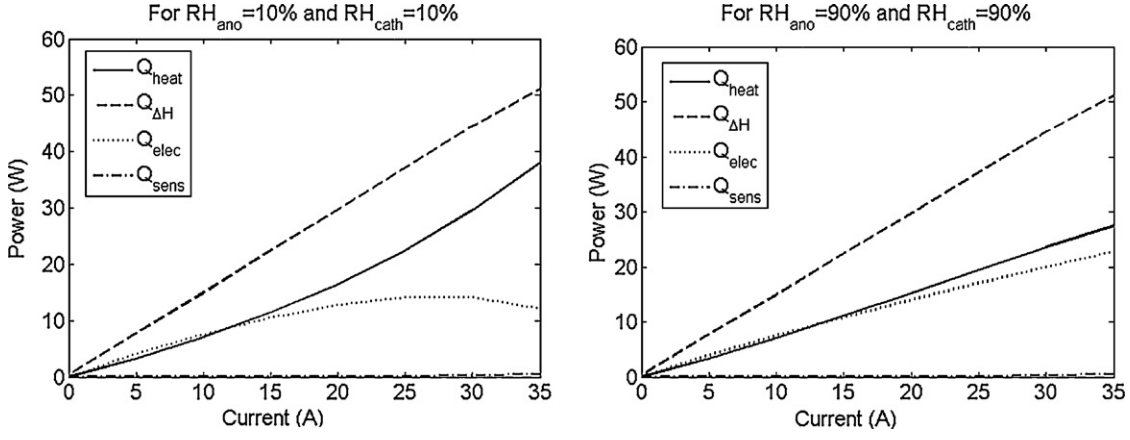

Fig. 5. Cell thermal power vs. load current $T_{\mathrm{cell}} = 70\,^{\circ}$C.

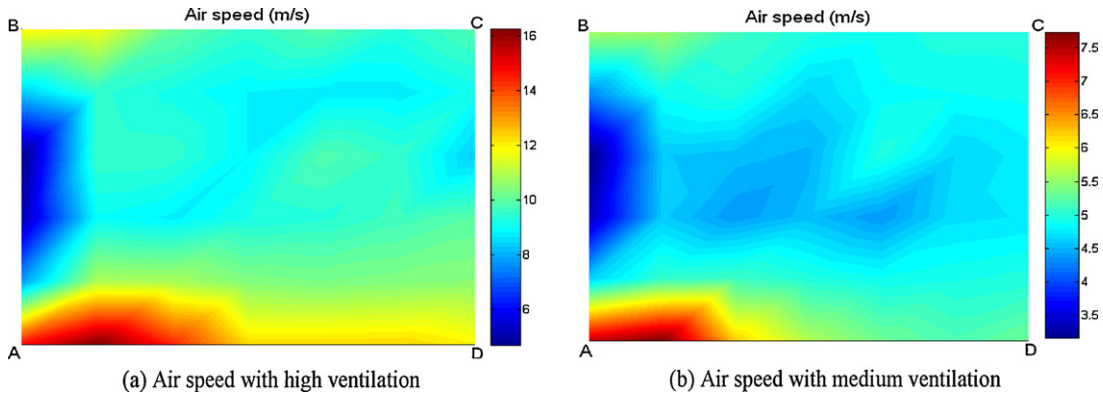

(a) Air speed with high ventilation (b) Air speed with medium ventilation

Fig. 6. Experimental air flow on top of the cell.

At high relative humidity ($RH_{ano} = RH_{cath} = 90\%$), the theoretical power splits into two comparable parts: the part converted into electricity and the part released as heat (see Eq. (1)). Moreover, at high currents, the energy released as heat (more than 27 W at 35 A) becomes more important than the energy converted into electricity (around 23 W at 35 A). On the other hand, at low gas humidification ($RH_{ano} = RH_{cath} = 10\%$), the electrical power is restricted to 14 W at 35 A because of the high membrane resistance (up to 0.78 $\Omega\,cm^2$ compared to 0.06 $\Omega\,cm^2$ with 90% relative humidity of the inlet gases). As a result, the power released as heat in the cell increases up to 38 W at 35 A. These figures show clearly that, with the exception of $\dot{Q}_{sens}$, the other three powers not only increase with the current, but that $\dot{Q}_{heat}$ and $\dot{Q}_{elec}$ depend noticeably on the inlet gas humidity. The simulation of the temperature profile in the cell is based on this model of the computed thermal power.

3.2. Boundary conditions of the cell thermal model

In order to analyze the efficiency of the cooling device, the air velocity was measured at the top of the cell stack, in the plane ABCD in Fig. 1 (where the stack length (AD, BC) is 56 cm and the stack width (AB, DC) is 25 cm) in maximum and medium ventilation conditions (Fig. 6—the numbers along the color scale on the right represent air velocity). The air velocity was measured with a mobile anemometer in 42 zones uniformly distributed over the top of the stack. The top surface is subdivided into seven regions along the stack length and six along the stack width.

Fig. 6 shows that the air flow is not uniform throughout the stack; some channels have a faster air flow than others. A comparison of Fig. 6a and b shows that the zones of highest and the lowest air flow remain in the same place even if the ventilation changes. The boundary conditions are therefore chosen to take this cooling non-uniformity into account. Different cooling channels are analyzed in order to represent the thermal behavior of the whole stack.

The boundary conditions in the thermal model are given by the temperatures measured in the cooling channel along the *y*-axis (vertical channel length axis). In order to analyze the thermal behavior of each cell in the stack, five sample channels have been chosen to analyze the temperature profile of the whole stack. The positions of the sample channels are shown in Fig. 7a. Channel 1 represents the lowest-cooled (due to lowest air flow) channel, whereas channel 5 represents the highest-cooled channel. For each of these channels, the temperature profiles are measured along the channel length. The air temperature measurements are used as boundary conditions in the thermal model. The tem-

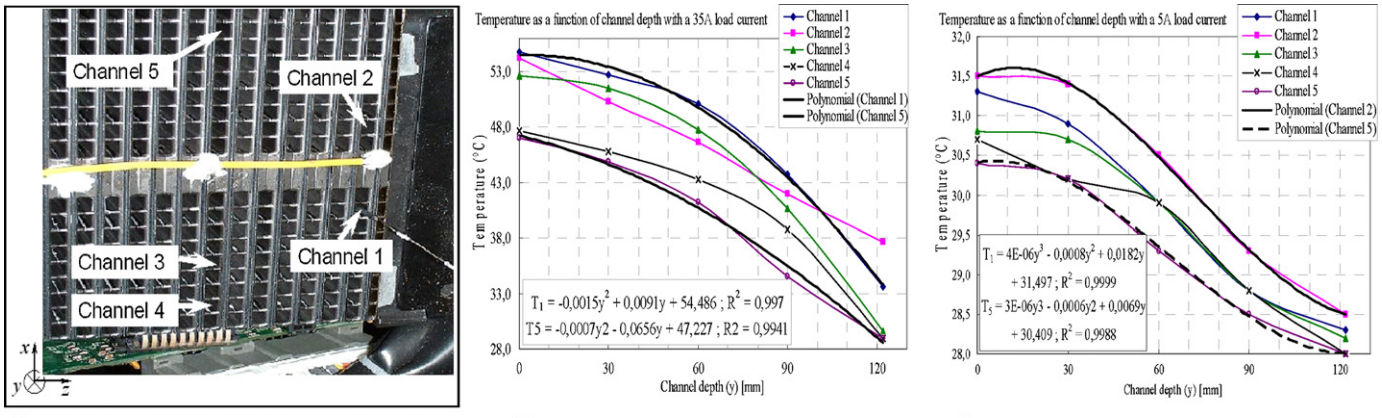

(a) (b) (c)

Fig. 7. Boundary conditions in sample channels: (a) Sample channel positions, (b) Channel temperature profile (with a 35 A current) and (c) Channel temperature profile (with a 5 A current).

perature profiles in these channels for 35 A and 5 A currents, as shown respectively in Fig. 7b and c, give the boundary conditions for the numerical analysis.

The measured temperatures in the channels allow a polynomial analytical estimation of the temperature profiles along the channels length (Fig. 7b and c).

As expected, the temperature increases along the cooling channels from bottom (right) to top (left) as air is heated inside the cell. The difference between outlet and inlet temperatures is typically about 3 °C at low current (Fig. 7b: channel 1 temperature increases from 28.3 °C to 31.3 °C), while it is about 23 °C at high current (Fig. 7c: channel 1 temperature increases from 33 °C to 55 °C). At high currents, the air flow is not sufficient for a convenient cooling of the cells, even though the fan is internally controlled by the system (higher air flow at higher load current). Such a large temperature gradient will result in a non-uniform temperature distribution throughout the cell. Moreover, at this high current, the non-uniform air ventilation leads to a 5 °C difference in air temperature between the channels, producing relatively great temperature non-uniformities throughout the stack (the corresponding figure at low current is about 1 °C). The use of water instead of air as a cooling fluid should reduce the temperature difference between inlet and outlet, since the specific heat of water is some 4000 times greater than that of air. This would produce smaller temperature gradients along the cells, resulting in smaller temperature variations between cells.

3.3. Steady-state thermal fields

Fig. 8 shows the computed simulation of the steady-state temperature field of a cell operated with a 35 A load current and at 90% relative humidity, and submitted to the lowest cooling intensity (channel 1). Fig. 8a–d show respectively the cell external temperature, the temperature field in the middle of the cell width (in the y–z plane), the temperature field in the middle of the cell thickness (x–y plane) and the temperature field in the middle of the cell depth (x–z plane). The lowest and highest temperatures in the cell are 67 °C and 70 °C respectively. The results show that along the y-axis, the temperature decreases from the top to the bottom because the cells are cooled from the bottom to the top. As expected, results also show that the center of the cell, including the membrane and the catalyst and diffusion layers, is hotter due to the thermal power generation inside the cell. The temperature field is symmetrical along the cell thickness due to the symmetrical cooling conditions on both sides of the cell.

It should be emphasized that the main purpose of this paper is more to analyze the influence of the cooling device on the thermal distribution (from bottom to top) along the cell, than

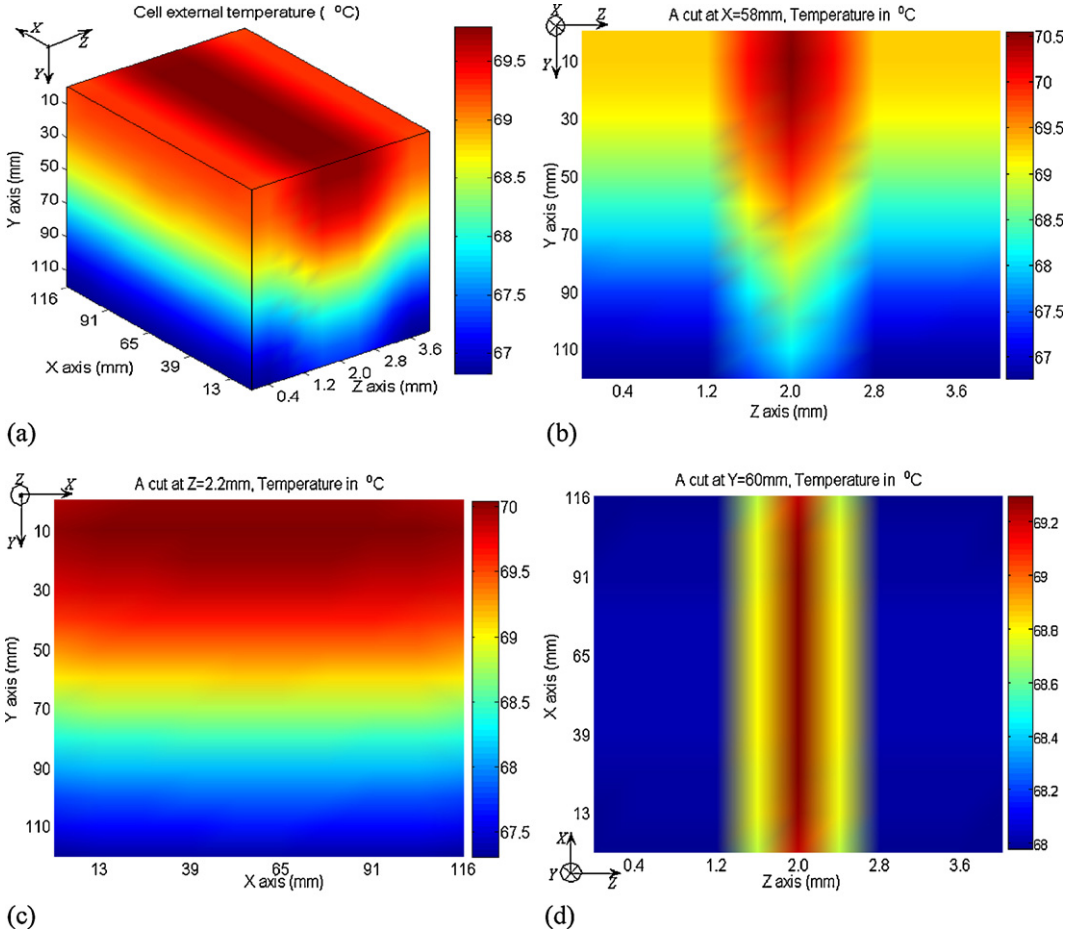

Fig. 8. Steady-state cell temperature field – 35 A load; current – channel 1: (a) Cell external temperature, (b) A cut at $x = 58$ mm, (c) A cut at $z = 2.2$ mm and (d) A cut at $y = 60$ mm.

to analyze internal 3D temperature profiles within the cell. This will help to anticipate its humidification (flooding and drying). In order to study the effect of air cooling magnitude, Fig. 9 repeats the simulation of Fig. 8 (cell operating at 35 A and at 90% relative humidity), but this time submitted to the highest cooling intensity, as seen in channel 5. In this case, the extreme temperatures are 59 °C and 62 °C (compared to 67.5 °C and 70 °C in the low-magnitude cooling of Fig. 8c). It thus appears that an increase of the cooling intensity does not have a strong effect on the internal cell temperature gradient. However, due to the better cooling, the fuel cell temperature decreases by about 8 degrees. Furthermore, the same observations about temperature fields and symmetries as in the previous case can be done.

By comparing the cell temperatures presented in Figs. 8 and 9, it appears that for a 35 A operating current and a 90% relative humidity, a temperature variation of 11 °C throughout the stack can be expected: 3 °C arising from the internal cell gradient and 8 °C from the temperature difference between the coolest and the warmest cells. This means that the different cells of the stack may have different electrochemical behavior due to their different temperatures. This remark is confirmed by [24], who reveals cell voltage variation in the stack, especially for the two cells nearest to the air compressor.

In the same electrical operating conditions as above but with a 10% relative humidity only, the shape of the temperature profile remains the same. However, the cell temperature ranges between 87 °C and 92 °C in the lowest cooling conditions and between 80 °C and 84 °C in the highest cooling conditions. As expected, the cell temperature increases due to the higher membrane resistance resulting in higher ohmic losses. The temperature gradient inside the cell therefore also increases up to 5 °C at 10% relative humidity instead of 3 °C with 90% relative humidity. Throughout the stack, the temperature gradient due to the non-uniform air cooling changes from 11 °C at 90% relative humidity to 12 °C at 10% relative humidity. Therefore, the influence of the relative humidity is significant in the cell, but is negligible from one cell to another.

The steady-state temperature field of a cell operated at 5 A was also studied. These results show that the predicted temperatures of the cell are fairly uniform around 32 °C, as measured experimentally by [24]. The temperature gradient does not exceed 0.5 °C throughout the cell. It can therefore be concluded that the higher the operating current, the higher the cell temperature and the more important the temperature gradients within the stack.

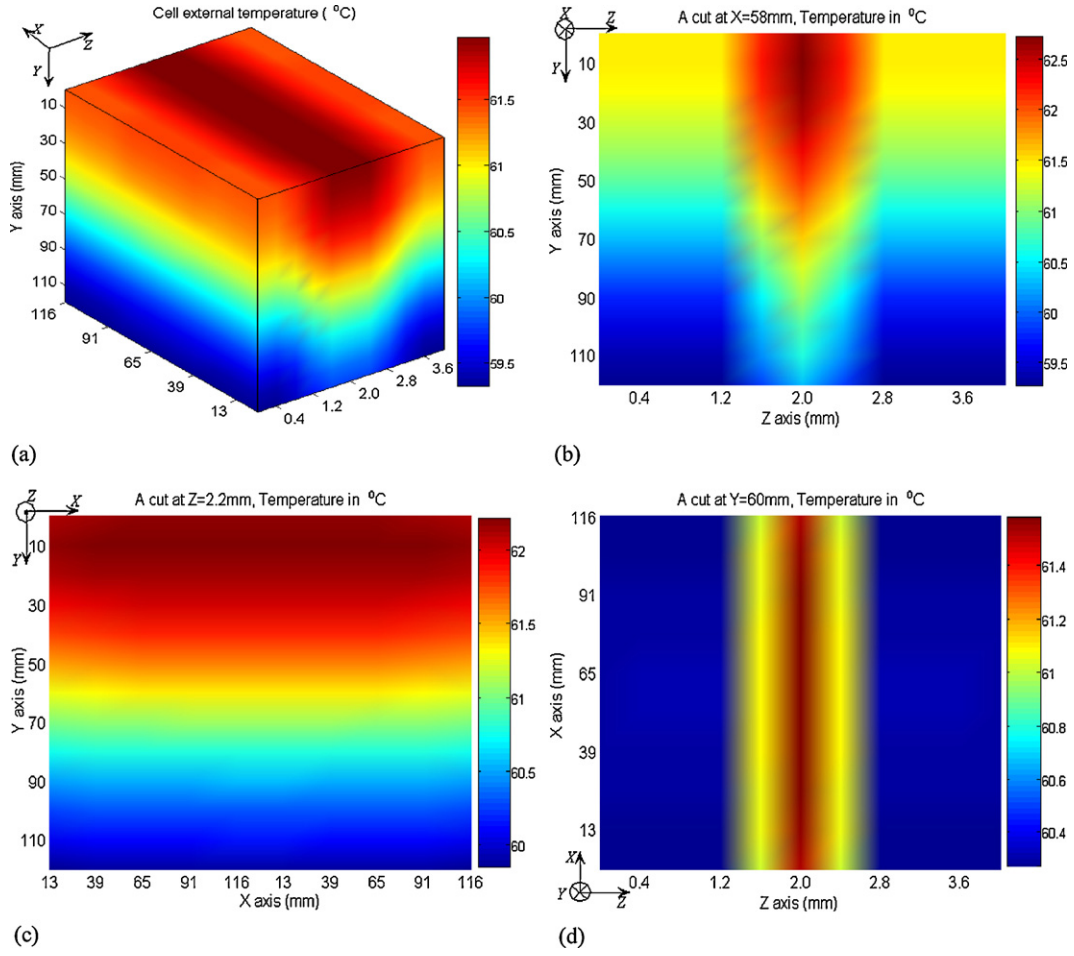

Fig. 9. Steady state cell temperature field – 35 A load current – channel 5: (a) Cell external temperature, (b) A cut at $x = 58$ mm, (c) A cut at $z = 2.2$ mm and (d) A cut at $y = 60$ mm.

3.4. Transient state thermal profile

The transient thermal response of the cell submitted to a load current demand variation from 5 A to 35 A with a 90% relative humidity is plotted in Fig. 10, according to the boundary conditions given by channel 1 (the highest temperature zone).

In this figure, the transient temperature in the centre of the cell is shown in Fig. 10a. Transient temperature profiles are plotted along three significant axes: along the cell thickness z, along the cell depth y, and along the cell width x.

The same conclusions concerning temperature distributions can be drawn as for the steady state case. Moreover, along the cell thickness (Fig. 10b), the temperature difference increases during the transient phase – because of the thermal power generation in the heart of the cell – and reaches its maximum of 2 °C at steady state (temperature at 1500 s in Fig. 10b). Along the cell depth (Fig. 10c), the temperature difference also increases in the transient phase and reaches its maximum of 3 °C at steady state (temperature at 1500 s in Fig. 10d). This is due to the ventilation going from the bottom to the top of the cell, thus implying a better cooling of the bottom than the top of the cell.

Even though the transient phase duration is up to 1500 s, it can be seen from Fig. 10a that the temperature reaches 99% of its steady state value after 900 s. These transient responses are pretty slow, so that thermal steady state should not be reached easily in transient operation of the cell.

3.5. Effect of the temperature on voltage

This study looks at the temperature variations in air cooled stacks, depending on the operating conditions. At low currents, the cell temperature is low (around 30 °C) and pretty uniform on the cell surface. However, an increase of the current leads to the increase of the mean cell temperature (up to 75 °C with a 90% relative humidity and up to 92 °C with a 10% relative humidity, at 35 A); it also leads to the increase of the local non-uniformity, as observed experimentally by [37]. As a result of this large temperature range, the electrical behaviors of the cell change. The influence of the local temperature variation on fuel cell voltage is emphasized in several publications [12,38]. Actually, mass and charge transfers strongly depend on temperature. The results also show that the gas humidities have a great impact on heat sources, and on temperature disparities in the cell. Low gas humidity results in high cell temperatures. And as the vapor saturation pressure depends on temperature, an increase in temperature reduces the gas relative humidity. This involves dryness of the membrane and consequently degradation in the cell voltage. All together this means that running a fuel cell with low inlet gas humidity can result in membrane failure if the cell is not properly cooled, especially at high current densities.

On the other hand, high gas humidities can result in flooding of the active layers, GDL and/or feeding channels. In the above temperature ranges, the saturation pressure is pretty low (only 0.043 bar at 30 °C); water condensation may therefore occur

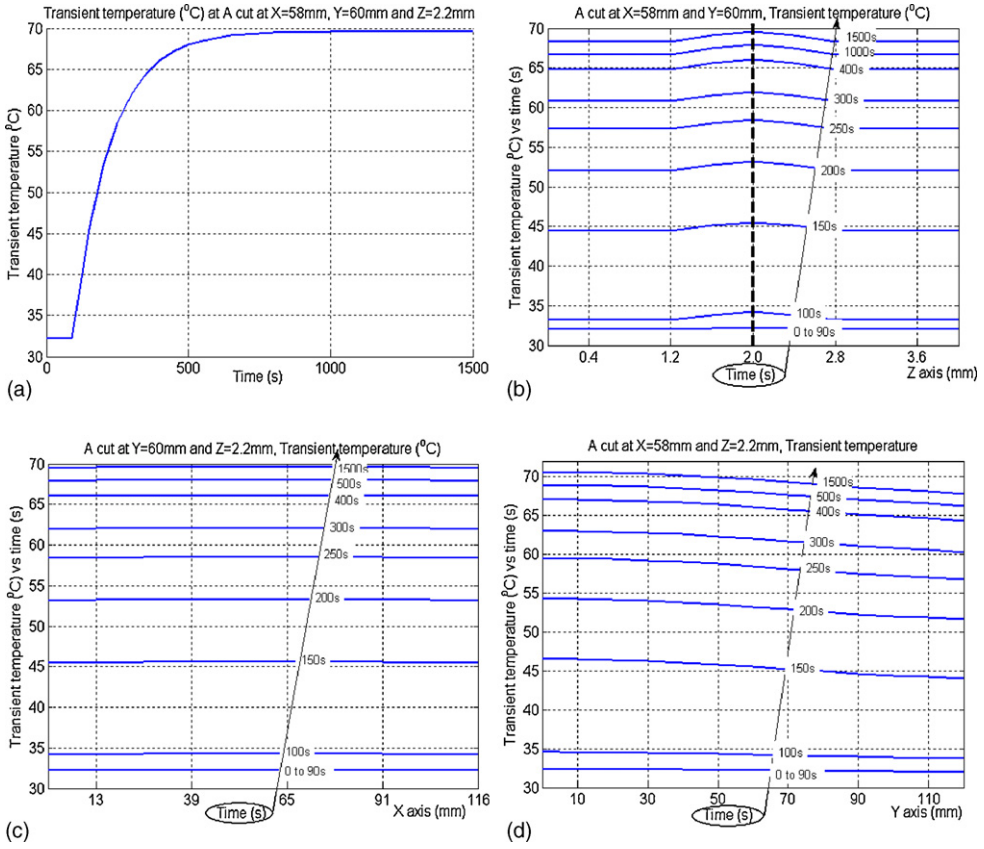

Fig. 10. Cell transient temperature profile – 35 A current – with a 5 A current as initial condition: (a) Temperature in the centre of the cell, (b) A cut at $X = 58$ mm and $Y = 60$ mm, (c) A cut at $X = 58$ mm $Z = 2.2$ mm and (d) A cut at $Y = 60$ mm and $Z = 2.2$ mm.

in the cell. A discussion about the preferential sites of water condensation is presented in [34] and descriptions of two-phase flows in a non-isothermal cell can be found in [39]. The authors insist on liquid water accumulation in the cell which drastically reduces the cell voltage at high currents and high gas humidity. Thus, the simulated cell potentials are intentionally not plotted here because the model does not yet take into account the water condensation phenomenon. Diphasic transport of water in the cell is currently under study. These remarks lead to the following statement for the air cooling device studied here: at high currents, the temperature difference between the top and the bottom of the cell could lead to membrane drying at the top because of the higher temperatures, and to water condensation at the bottom due to the lower temperatures. Moreover, water condensation at the bottom would be increased due to the gravity. So, large voltage losses can be encountered in the whole cell because of the temperature non-uniformity. Moreover, the disparities in cooling air velocities from one cell to another are also pointed out. This implies that cells in the stack have different electrochemical behaviors depending on their temperature. Thus, some cells in the stack are more subjected to drying while, at the same time, some others are subjected to flooding. It follows that the cooling device for the NEXA stack has to be improved to keep the cell at its optimal temperature.

4. Conclusions

The aim of this study is to characterize the influence of the air cooling device on fuel cell performances. To reach this goal, a dynamic 3D thermal modeling of a proton exchange membrane fuel cell is presented. The model includes the natural convection due to ambient air cooling, the forced convection due to the stack ventilation, and the influence of the thermal power generation inside each cell. The gas humidity shows a great impact on membrane resistance, resulting in higher heat generation in the cell. Different air flow zones are studied to understand the thermal behavior of the cells. This model brings out the temperature non-uniformity throughout the stack. The "NEXA" fuel cell stack of Ballard Power Systems was used to validate the approach.

In the cell depth direction, the temperature difference between the top and the bottom of the cell reaches its maximum of 5 °C at steady state at 35 A. This difference is linked to the air ventilation from the bottom to the top of each cell. Moreover, the influence of the load current on the mean cell temperature is also emphasized. For instance, the temperature of the cell, fed with high-humidified gases, is around 30 °C for a 5 A load current and around 70 °C for a 35 A load current. With low gas humidity, the total heat production rises, resulting in higher temperatures in the cell (up to 92 °C at 35 A). The results also demonstrate temperature non-uniformity in the stack, which increases with the load current: 3–5 °C difference in the cell and up to 7–8 °C difference between the cells, due to the cooling non-uniformity at 35 A. Finally, the influence of such temperature differences on electrical performances is analyzed. The temperature distribution is responsible for electrical disparities in the cell depth and from one cell to another. Moreover, the temperature field tends to involve water condensation at the bottom and membrane dehydration at the top. This results in cell voltage disparities, which reduces the global electrical power produced by the stack. This characterization will be useful for an efficient control of the fuel cell stack.

Acknowledgement

This work was jointly supported by LTE-Hydro-Quebec and Natural Sciences and Engineering Research Council of Canada.

References

[1] T. Berning, D.M. Lu, N. Djilali, J. Power Sources 106 (2002) 284–294.
[2] W.-M. Yan, F. Chen, F. Chen, H.-Y. Wu, C.-Y. Soong, H.-S. Chu, J. Power Sources 129 (2004) 127–137.
[3] A. Biyikoglu, Int. J. Hydrogen Energy 30 (2005) 1181–1212.
[4] L. Dumercy, R. Glises, H. Louahlia-Gualous, J.M. Kaufmann, J. Power Sources 156 (2006) 78–84.
[5] D.B. Genevey, M.R. von Spakovsky, M.W. Ellis, D.J. Nelson, B. Olsommer, F. Topin, N. Siegel, N. Montel, International Mechanical/ Engineering Congress and Exposition—IMECE'2002, New York, NY, November, 2002, ASME Paper no. 33322.
[6] C. Wang, M.H. Nehrir, S.R. Shaw, IEEE Trans. Energy Convers. 20 (2005) 442–451.
[7] W.-M. Yan, C.-Y. Soong, F. Chen, H.-S. Chu, J. Power Sources 143 (2005) 48–56.
[8] M.J. Khan, M.T. Iqbal, Fuel Cells 5 (2005) 463–475.
[9] Y. Zhang, M. Ouyang, Q. Lu, J. Luo, X. Li, J. Therm. Eng. 24 (2004) 501–513.
[10] H. Meng, J. Power Sources 171 (2007) 738–746.
[11] P.T. Nguyen, T. Berning, N. Djilali, J. Power Sources 130 (2004) 149–157.
[12] H. Wu, P. Berg, X. Li, J. Power Sources 165 (2007) 232–243.
[13] Y. Shan, S.-Y. Choe, J. Power Sources 145 (2005) 30–39.
[14] X. Xue, J. Tang, A. Smirnova, R. England, N. Sammes, J. Power Sources 133 (2004) 188–204.
[15] S. Shimpalee, S. Greenway, J.W. Van Zee, J. Power Sources 160 (2006) 398–406.
[16] Y. Wang, C.-Y. Wang, J. Power Sources 153 (2006) 130–135.
[17] S. Shimpalee, D. Spuckler, J.W. Van Zee, J. Power Sources 167 (2007) 130–138.
[18] J.J. Hwang, C.H. Chao, W.Y. Ho, C.L. Chang, D.Y. Wang, J. Power Sources 157 (2006) 85–97.
[19] J.-H. Koh, A.T. Hsu, H.U. Akay, M.-F. Liou, J. Power Sources 144 (2005) 122–128.
[20] Y.-J. Sohn, G.-G. Park, T.-H. Yang, Y.-G. Yoon, W.-Y. Lee, S.-D. Yim, C.-S. Kim, J. Power Sources 145 (2005) 604–609.
[21] J.H. Lee, T.R. Lalk, A.J. Appleby, J. Power Sources 70 (1998) 258–268.
[22] J.C. Amphlett, R.F. Mann, B.A. Peppley, P.R. Robergel, J. Power Sources 61 (1996) 183–188.
[23] Y. Shan, S.-Y. Choe, J. Power Sources 158 (2006) 274–286.
[24] W.H. Zhu, R.U. Payne, D.R. Cahela, B.J. Tatarchuk, J. Power Sources 128 (2004) 231–238.
[25] A.J. del Real, A. Arce, C. Bordons, J. Power Sources 173 (2007) 310–324.
[26] M. Fournier, K. Agbossou, A. Poulin, Y. Dubé, G. Simard, Proceedings of the 16th World Hydrogen Energy Conference, Lyon France, 13–16 June, 2006.
[27] L. Jia, Z. Su, B. van den Hurk, M. Menenti, A. Moene, H.A.R. De Bruin, J.J.B. Yrisarry, M. Ibanez, A. Cuesta, Phys. Chem. Earth 28 (2003) 75–88.
[28] B. Dhifaoui, S.B. Jabrallah, A. Belghith, J.P. Corriou, Int. J. Therm. Sci. 46 (2007) 1056–1063.
[29] F. Barbir, PEM Fuel Cells: Theory and Practice, Elsevier Academic Press, New York, 2005.

[30] A. Poulin, M. Dostie, S. Martel, Fuel Cell Seminar in San Antonio, Texas, 1–5 November, 2004.
[31] S. Cleghorn, J. Kolde, W. Liu, Catalyst Coated Composite Membranes, of Handbook of Fuel Cells—Fundamentals Technology and Applications, vol. 3, John Wiley & Sons, Chichester, 2003 (Chapter 44, Part 3, pp. 566–575.
[32] J.C. Amphlett, R.M. Baumert, R.F. Mann, B.A. Peppley, P.R. Roberge, J. Electrochem. Soc. 142 (1) (1995) 1–8.
[33] R.B. Bird, W.E. Stewart, E.N. Lightfoot, Transport Phenomena, John Wiley & sons, New York, 1960.
[34] T.E. Springer, T.A. Zawodzinski, S. Gottesfeld, J. Electrochem. Soc. 138 (8) (1991) 2334–2342.
[35] J. Ramousse, S. Didierjean, O. Lottin, D. Maillet, Int. J. Therm. Sci. 47 (2008) 1–6.
[36] M. Khandelwal, M.M. Mench, J. Power Sources 161 (2006) 1106–1115.
[37] M. Wang, H. Guo, C. Ma, J. Power Sources 157 (2006) 181–187.
[38] W.-M. Yan, F. Chen, H.-Y. Wu, C.-Y. Soong, H.-S. Chu, J. Power Sources 129 (2004) 127–137.
[39] L. Matamoros, D. Brüggemann, J. Power Sources 161 (2006) 203–213.